Neuron
Neurotechnique

Supraresolution Imaging in Brain Slices using Stimulated-Emission Depletion Two-Photon Laser Scanning Microscopy

Jun B. Ding,[1] Kevin T. Takasaki,[2] and Bernardo L. Sabatini[1,*]
[1]Department of Neurobiology, Howard Hughes Medical Institute, Harvard Medical School, Boston, MA 02115, USA
[2]Program in Biophysics, Harvard University, Cambridge MA 02138, USA
*Correspondence: bsabatini@hms.harvard.edu
DOI 10.1016/j.neuron.2009.07.011

SUMMARY

Two-photon laser scanning microscopy (2PLSM) has allowed unprecedented fluorescence imaging of neuronal structure and function within neural tissue. However, the resolution of this approach is poor compared to that of conventional confocal microscopy. Here, we demonstrate supraresolution 2PLSM within brain slices. Imaging beyond the diffraction limit is accomplished by using near-infrared (NIR) lasers for both pulsed two-photon excitation and continuous wave stimulated emission depletion (STED). Furthermore, we demonstrate that Alexa Fluor 594, a bright fluorophore commonly used for both live cell and fixed tissue fluorescence imaging, is suitable for STED 2PLSM. STED 2PLSM supraresolution microscopy achieves approximately 3-fold improvement in resolution in the radial direction over conventional 2PLSM, revealing greater detail in the structure of dendritic spines located ~100 microns below the surface of brain slices. Further improvements in resolution are theoretically achievable, suggesting that STED 2PLSM will permit nanoscale imaging of neuronal structures located in relatively intact brain tissue.

INTRODUCTION

Fluorescence microscopy has been widely used in neuroscience research and has revealed the complex and dynamic structure and function of the brain. This technique has been applied to many different spatial scales, from mapping neural circuits (millimeters to centimeters) to resolving individual synapses (~1 μm). However, conventional wide-field and confocal microscopy are not well suited to imaging structures below the surface of brain tissue, where scattering, absorption, and out-of-focus fluorescence degrade the signal of interest. Two-photon laser scanning microscopy (2PLSM) allows the use of tissue-penetrating, near-infrared wavelengths to achieve multiphoton excitation restricted to the focal plane (Denk and Svoboda, 1997; Svoboda and Yasuda, 2006). The application of 2PLSM to neurobiology has allowed unprecedented high-resolution fluorescence imaging within scattering tissue and has been used, for example, to visualize the morphological plasticity of dendritic spines in living animals, to study the properties of individual synapses in brain slices, and to examine microscale biochemical signaling within neurons (Denk et al., 1994; Lee et al., 2009; Lendvai et al., 2000; Sabatini and Svoboda, 2000; Tanaka et al., 2008; Yuste and Denk, 1995).

However, many features of neurons are too small to be resolved by confocal microscopy and 2PLSM. These include many synaptic structures such as filopodia and thin dendritic spines, nearly all dendritic spine necks, the structure of the postsynaptic density, and the organization of the presynaptic terminal (Bourne and Harris, 2008; Shepherd and Harris, 1998). The limit of spatial resolution in light microscopy, or the "diffraction limit," was described by Ernst Abbe (Abbe, 1873), who stated that the resolution (d) is limited by the wavelength of light (λ) and the numerical aperture (NA) of the lens such that $d = \lambda/2NA$. With confocal fluorescence microscopes, thin specimens can be imaged with resolution of ~150 nm by using short wavelength (~400 nm) excitation light and high NA oil-immersion objectives. In contrast, near-infrared (NIR) photons of 750–950 nm are necessary for tissue penetration and excitation in 2PLSM. In addition, imaging neurons in living brains or brain slices requires the use of lower NA water-immersion lenses. For these reasons, the resolution of 2PLSM is 2- to 3-fold worse than that of conventional confocal microscopy and is typically ~400–500 nm.

Several methods have been described that allow imaging below the diffraction limit (i.e., supraresolution imaging; Betzig et al., 2006; Gustafsson, 2005; Hell and Wichmann, 1994; Kner et al., 2009; Rust et al., 2006). Unfortunately, current implementations of these approaches suffer resolution degradation if emitted photons are anisotropically scattered and thus have only been applied in nonscattering environments or near the surface of scattering tissue. However, the supraresolution methodology stimulated emission depletion (STED) microscopy (Hell and Wichmann, 1994) is theoretically insensitive to scattering of emitted photons if fluorophore excitation is achieved via multiphoton processes. Thus, a microscope that uses near-infrared photons to perform both two-photon excitation and one-photon STED may be suitable for supraresolution imaging within brain tissue.

STED microscopy circumvents the diffraction limit by constricting the population of excited fluorophores to a region

smaller than the focal spot via a saturable and reversible electronic transition (Kittel et al., 2006; Willig et al., 2006). STED microscopy uses a coaligned pair of focused laser beams, one for excitation and a second to deplete the excited state by forcing nonfluorescent decay back to the ground state. The phase of the depletion laser beam is spatially patterned such that it produces an annular illumination pattern in the specimen plane and suppresses fluorescence in the periphery of the excitation volume. The resolution is no longer strictly limited by λ and NA but is given by

$$d = \frac{\lambda}{2NA\sqrt{1 + I/I_{sat}}} \quad (1)$$

where I is the power of the depletion laser and I_{sat} is a fluorophore-dependent parameter corresponding to the laser power required to deplete 50% of the fluorescence (Hell et al., 2004).

STED microscopy using one-photon excitation has achieved resolutions of ~20–50 nm and, within neuroscience research, has been used to determine the location of fluorescent antibody labeled proteins in fixed tissue, to observe the movement of neurotransmitter vesicles inside dissociated neurons and to image dendritic spines at the surface of the brain (depth < 10 μm) (Eggeling et al., 2009; Nagerl et al., 2008; Westphal et al., 2008).

Here, we demonstrate supraresolution fluorescence imaging deep within brain tissue using one-photon near-infrared STED of two-photon excited fluorophores. We use "deep" to refer to depths beyond the scatter length of visible photons, where performance of single photon imaging is substantially degraded. We find that two-photon excited fluorophores can be depleted by one-photon processes and that annular illumination patterns can be formed using water-immersion objectives despite the index of refraction mismatch between the immersion solution and the tissue. Furthermore, Alexa Fluor 594, a commonly used and bright water-soluble red fluorophore, has properties suitable for pulsed two-photon excitation and continuous wave one-photon STED. Thus, supraresolution imaging based on combined stimulated emission depletion and two-photon laser scanning microscopy (STED 2PLSM) is theoretically feasible for deep tissue imaging. Implementing this approach, we image whole-cell voltage-clamped neurons in acute brain slices at resolutions ~3-fold beyond the Abbe diffraction limit. The shape of small spines and filopodia and the width of spine necks located deep within the brain slice can be more accurately resolved and measured, revealing significantly greater detail than detectable by standard two-photon microscopy. Thus, STED 2PLSM provides an imaging modality for supraresolution imaging within scattering brain tissue and, with further improvement in efficient depletion power delivery, will allow nanoscale imaging within complex tissues.

RESULTS

Two-Photon Excitation and One-Photon CW STED

In order to determine if STED can be combined with 2PLSM to achieve supraresolution two-photon imaging in brain tissue, we examined if fluorophores excited via two-photon processes can be forced to the ground state via nonfluorescent one-photon STED (Figure 1). Crimson fluorescent beads embedded in mounting media were imaged using a pulsed Ti:sapphire laser tuned to 840 nm for two-photon excitation (Figure 1A). Transient illumination with a second Ti:sapphire laser operating in continuous wave (CW) mode and tuned to 760 nm instantly and reversibly suppressed fluorescence in a power-dependent manner (Figures 1B and 1C). Such instantaneously reversible reduction of fluorescence by illumination with light in the long-wavelength portion of the emission spectrum is consistent with STED of the two-photon excited state (Figure 1D). As expected, fluorescence was a function of STED illumination power of the form $(1+\gamma P_{sted})^{-1}$, with γ representing a constant. The power necessary for depletion of 50% of the fluorescence signals (I_{sat}) was 87.5 mW and at the peak intensity of STED illumination (591 mW), the fluorescence of the bead was suppressed greater than 10-fold (Figure 1E). Thus, fluorescence generated via two-photon processes can be efficiently suppressed via nonfluorescent stimulated depletion with NIR light.

Live neuron imaging in brain slices has benefited from the use of bright, highly water-soluble fluorescent indicators such as the Alexa series of fluorophores. Based on its emission tail beyond 700 nm, its long fluorescent state lifetime (3.9 ns; Invitrogen), and its efficient two-photon excitation, we predicted that Alexa Fluor 594, a red fluorophore commonly introduced into living neurons via whole-cell recording pipettes, would be suitable for STED 2PLSM. An aqueous solution of Alexa 594 (50 μM) in a sealed patch-clamp recording pipette (Figure 1F) fluoresced brightly upon two-photon excitation at 840 nm. Fluorescence was instantaneously and reversibly suppressed on illumination with a CW laser at 736 nm. Fluorescence recovery was instantaneous when the 736 nm laser was switched off, consistent with nonfluorescent depletion of the excited state (Figures 1G and 1H). At maximum STED laser power, the fluorescence was depleted to less than 10% of maximal with I_{sat} = 34.8 mW (Figures 1I and 1J). These results indicate that two-photon excited Alexa 594 is depleted at low power levels compatible with live-cell imaging and thus may be a suitable fluorophore for supraresolution two-photon imaging of living neurons.

Design of a Combined STED 2PLSM Microscope

Supraresolution imaging STED microscopy requires illumination of the specimen with a phase-patterned laser beam that selectively suppresses fluorescence from fluorophores located in the outer shells of the excitation volume. For this reason supraresolution STED microscopy requires that the phase of illumination be fixed in space and is not compatible with the nonstationary illumination of the back-focal plane of the objective found in most implementations of laser-scanning microscopes. In published reports of supraresolution STED microscopy, the fixed phase/space relationship is accomplished by moving the specimen, in at least one axis, under the objective instead of scanning the illumination beam through the tissue (Willig et al., 2006). This results in slow scanning speeds (20–40 s/frame) that are challenging for live-cell imaging (Nagerl et al., 2008). We built a laser scan head that creates a stationary pattern of illumination in the objective back focal plane by making this plane optically conjugate to both scan mirrors (Figure 2). This was accomplished using a planoconvex lens and a curved silver

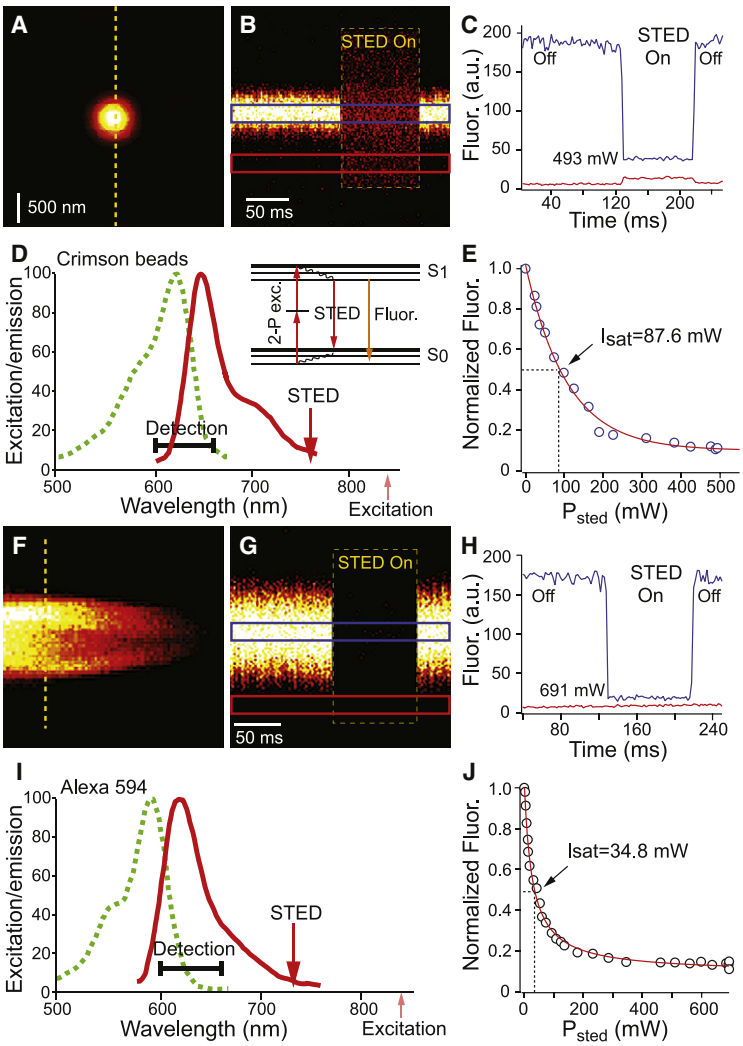

Figure 1. Depletion of Two-Photon Excited Fluorophores with Continuous-Wave Near-Infrared Light

(A) Image of a 200 nm diameter crimson fluorescent bead (Crimson carboxylate-modified FluoSpheres) acquired with 2PLSM at excitation wavelength of 840 nm.

(B) Fluorescence measured in line scans over the region indicated by the dashed line in (A) during normal excitation and with additional illumination with 760 nm light (boxed region).

(C) Quantification of fluorescence intensity in the regions of interest (ROI) indicated by the colored boxes in (B). Despite maintained two-photon excitation, turning on the STED beam reduces fluorescence from the bead (blue). In addition, a small amount of background signal is present (red) when the depletion laser is active.

(D) Absorption and emission spectrum of crimson beads. The depletion wavelength (760 nm) is in the low energy (long wavelength) portion of the emission spectrum. Insert: Simplified energy diagram of two-photon excitation and one-photon depletion. A molecule is excited from the ground state S0 into an excited state S1. It can return to the ground state by spontaneous emission of a photon (fluorescence) or by stimulated emission of a photon that is coherent with the depletion light.

(E) Relative fluorescence intensity of crimson fluorescent beads under two-photon excitation at 840 nm as a function of the depletion laser power (P_{sted}) at 760 nm. The power required for suppression of 50% of fluorescence is indicated.

(F) 2PLSM image of a sealed glass pipette filled with 50 μM Alexa 594 in aqueous solution.

(G) Fluorescence of Alexa 594 measured in line scans over the region indicated by the dashed lines in (F) during normal excitation and with additional illumination with CW 736 nm light (boxed region).

(H) Quantification of fluorescence intensity in the ROI indicated by the colored boxes in (G).

(I) One-photon excitation and fluorescence emission spectra of Alexa 594 indicating the depletion wavelength of 736 nm in the far red region of the emission spectrum.

(J) Depletion of Alexa 594 fluorescence under constant two-photon excitation with 840 nm light as a function of the power (P_{sted}) of applied 736 nm depletion light.

mirror that maintain laser collimation while imaging one scanning galvanometer mirror onto the second (Figure 2A). This optical arrangement also improves laser power delivered into the objective by reducing the degree of overfilling of the back-aperture necessary to maintain imaging resolution (Tsai et al., 2002).

Introduction of a vortex phase plate and quarter wave plate (1/4λ) into the optical path (Figure 2B) produced the annular STED illumination pattern in the specimen plane necessary for supraresolution imaging (Eggeling et al., 2009). By placing the STED laser into mode-locked (i.e., pulsed) mode and imaging crimson beads, the profiles of the STED and excitation beams could be measured in the specimen plane. Furthermore, using this optical design, the concentric illumination patterns can be scanned through the sample without requiring movement of the stage (Figure 2C).

Supraresolution Two-Photon Imaging Achieved with STED 2PLSM

To demonstrate the ability of STED 2PLSM to image with sub-diffraction limited resolution, we used the above optical configuration to image clusters of fluorescent beads by 2PLSM with the CW STED laser on or off (Figure 3). Comparison of 2PLSM and STED 2PLSM reveals an improvement of radial resolution when the STED laser is activated (Figures 3A and 3B). Under conventional 2PLSM imaging, fluorescence images of 200 nm diameter crimson beads displayed an average full-width at half maximum (FWHM) of 530 nm. In contrast, STED 2PLSM images exhibited an average FWHM of 280 nm, indicating a greater than 2-fold improvement in resolution. Furthermore, STED 2PLSM improved the capability to resolve fluorescent structures in close proximity, including beads separated by less than 500 nm (Figures 3C–3G). Lastly, the sharpness of the edges of beads was greater for STED 2PLSM than for 2PLSM images. This was quantified by measuring the maximal rate of change of fluorescence in each line of the image (see Figure S1 available online). The maximal spatial derivative of the fluorescence normalized by the cumulative fluorescence intensity (%ΔF/nm) was larger for STED 2PLSM than for 2PLSM images, consistent with improved imaging resolution.

Live-Cell Imaging of Dendrites and Spines

A technical limitation that may hinder the application of STED 2PLSM to deep brain imaging comes from the mismatch of the

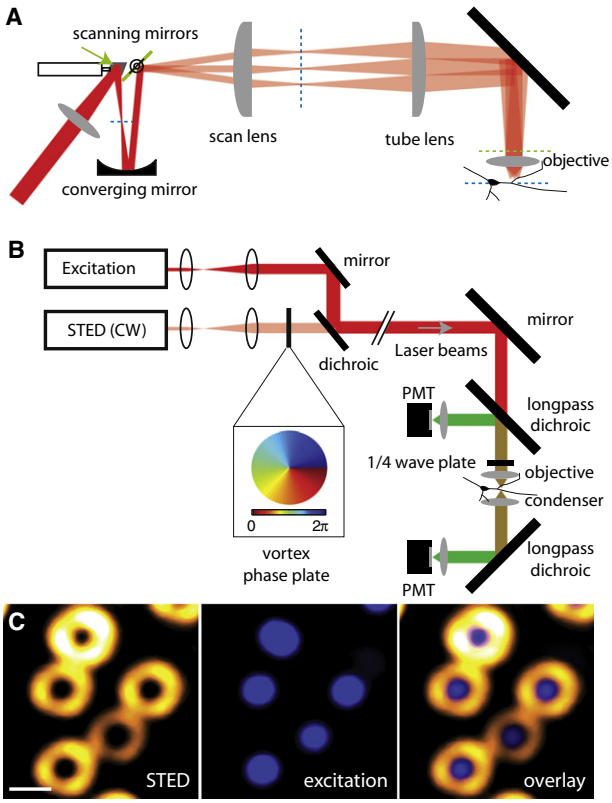

Figure 2. Schematic of the STED 2PLSM Optical Path

(A) Schematic of the microscope scan head. This design places both scan mirrors and the back focal plane of the objective in conjugate optical planes and creates a stationary illumination at the back-focal plane of the objective. The dashed blue lines indicate planes conjugate to the image whereas the dashed green lines and arrow represent planes conjugate to the objective back focal plane.

(B) Schematic of the optical path for modulation and combination of the two-photon excitation (dark red) and one-photon depletion (light red) laser light. The depletion laser beam is passed through a vortex phase plate ($0 \leq \Phi \leq 2\pi$ phase modulation) before combination with the excitation light at a dichroic. Both epifluorescence and transfluorescence are collected by photomultiplier tubes (PMT). The $\frac{1}{4}$ wave plate circularly polarizes the excitation and STED light.

(C) 2PLSM images of crimson beads collected with the phase patterned depletion laser (left, yellow) and the excitation laser (middle, blue). The superimposition of these (right) illustrates the annular distribution of depletion light in the focal plane around the excitation volume. Scale bar, 500 nm.

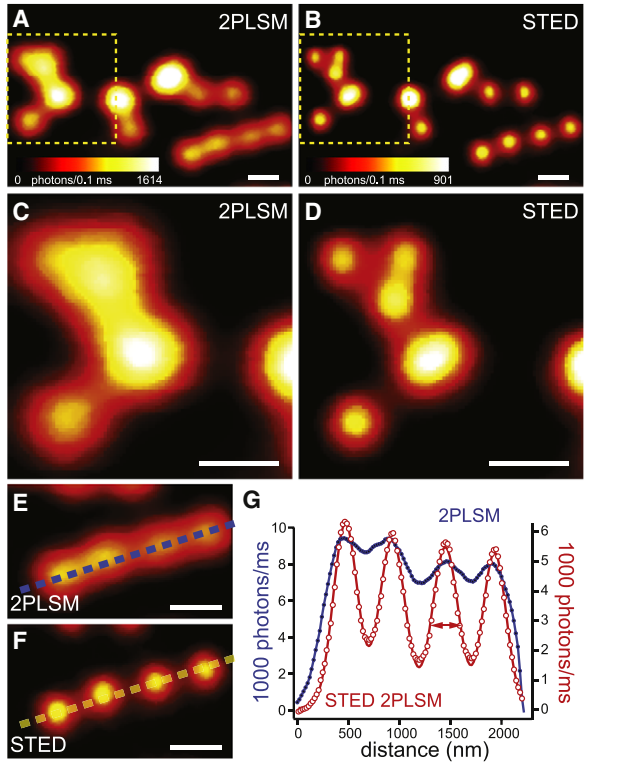

Figure 3. Supraresolution Two-Photon Imaging Achieved with STED 2PLSM

(A and B) Images of fluorescent 200 nm crimson beads acquired with 2PLSM (A) and STED 2PLSM (B). The images were collected simultaneously by switching the STED laser on and off in alternate lines of the image at 500 Hz.

(C and D) Enlarged images of the boxed areas in (A) and (B), respectively, demonstrating the improved resolving power of STED 2PLSM compared to 2PLSM.

(E and F) Enlarged images of the linear cluster of beads in (A) and (B) acquired with (E) and without (F) the STED laser active.

(G) The profile of fluorescence intensity along the dashed lines in (E) and (F) exhibits clear separation of clustered fluorescent beads in the STED 2PLSM mode (red) but not in the 2PLSM mode (blue). The STED 2PLSM fluorescence profile was fit (red line) to the sum of four Gaussians with identical widths (FWHM = 300 nm) and a separation of 500 nm. Scale bars, 500 nm in all images.

refractive indices between the immersion medium (water, ~1.34) and the brain tissue (~1.41). Such mismatches may result in spherical aberration that reduces the ability of the STED beam to form an annular profile with a zero-intensity center. To explore this possibility, we imaged crimson beads in poly(dimethyl siloxane) (PDMS, Sylgard 184), which has a similar index of refraction (~1.41–1.43) to that of brain tissue (Yan et al., 2007). The annular distribution of the focused STED beam was maintained 200–250 μm deep in PDMS (Figure S2) without degradation of the zero-intensity center. This indicates that index of refraction mismatches do not limit supraresolution tissue imaging with STED 2PLSM.

To test the applicability of STED 2PLSM to live-cell imaging in brain tissue, we performed fluorescence imaging of CA1 hippocampal pyramidal neurons in mouse acute brain slices. Neurons were filled with Alexa 594 (100 μM) through a whole-cell patch clamp recording pipette and dendritic spines were imaged under 2PLSM and STED 2PLSM imaging modes (Figure 4). For spines located 30–110 μm below the surface of the slice, STED 2PLSM revealed significantly greater detail than 2PLSM (Figure 4A).

Quantification of the effective resolution of an imaging modality is difficult to extract from images of objects with an a priori unknown structure. However, improvements in resolution resulting from STED 2PLSM were evident from several features of the images. First, objects that appeared fused in 2PLSM were resolved as distinct objects by STED 2PLSM. This includes visualization of the separation between spine heads and parent dendrite, between closely spaced filopodia, and identification

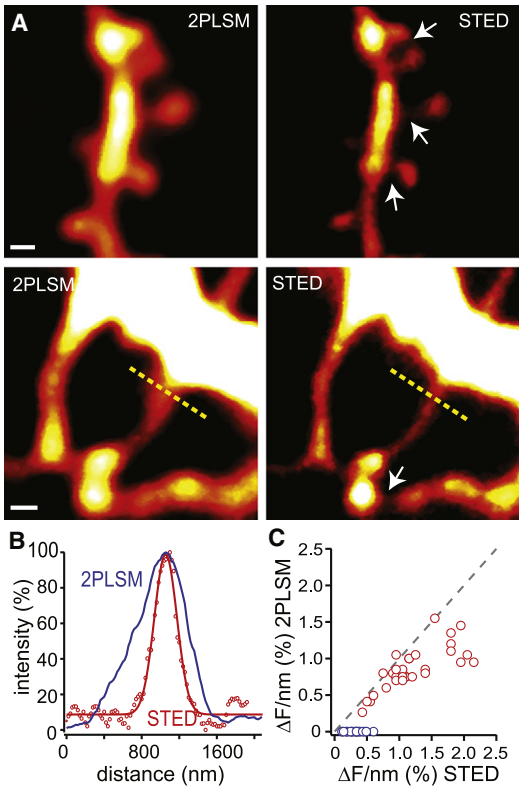

Figure 4. STED 2PLSM Images of Dendritic Spines Deep in Brain Tissue

(A) Image pairs of dendritic spines acquired with 2PLSM (left) and STED 2PLSM (right). CA1 pyramidal neurons in acute hippocampal slices were filled with 100 μM Alexa 594 through a whole-cell recording pipette. The images were acquired simultaneously by switching the STED laser on and off in alternate lines at 500 Hz. The arrows indicate details in the STED image that are not resolved in 2PLSM. Scale bars, 500 nm in all images. The dendrites were located at approximate depths of 80 μm (top) and 45 μm (bottom) below the surface of the slice.

(B) The profiles of fluorescence intensity along the dashed lines in (A) demonstrate improved resolution of the spine neck in STED 2PLSM mode (red) compared to in 2PLSM mode (blue). The line profile of the spine neck in the STED image was fit to a Gaussian with FWHM = 280 nm.

(C) Plot of the maximum rate of fluorescence changes in 2PLSM and STED 2PLSM images. In order to allow for comparison of images with different fluorescence intensities, the rate of change of fluorescence is expressed as a percent change per nm relative to total integrated fluorescence (%ΔF/nm). For objects that can be accurately sampled by 2PLSM there should be no increase in the measured parameter when the same structure is imaged by STED 2PLSM. These points should lie along the line of unity (dashed line). In contrast, for structures that are below the resolution limit of 2PLSM, the rate of change of fluorescence should increase under STED 2PLSM as the blurring or low-pass filtering effect of low resolution is reduced. The blue points indicate regions of detail that are evident only in the STED 2PLSM images.

of multiple spines within indistinct fluorescence blobs. Second, the cross-sectional profile of thin objects such as filopodia was narrower in STED 2PLSM than in 2PLSM such that the full-width at half-maximum (FWHM) was reduced from 660 to 280 nm (Figure 4B). Assuming the flipodium has a circular cross-section with a diameter of 100–200 nm, this corresponds to an ~3-fold increase in resolution. Lastly, as revealed by the analysis of maximal rates of change of fluorescence described above, the sharpness of large objects such as mushroom spines and dendrites, was greater for STED 2PLSM than for 2PLSM images (Figures 4C and S3). This analysis indicates improved resolution that, as expected, is most evident for structures of high spatial frequency. The improved two-object discrimination and the increased sharpness of spine images as well as the FWHM of fluorescent beads were dependent on the STED illumination intensity, as expected for this imaging modality (Equation 1 and Figure S4).

Improved Analysis of Spine Morphology with STED 2PLSM

The current implementation of STED 2PLSM improves resolution in lateral dimensions but not along the axial (z) axis. In order to understand if the increased lateral resolution is sufficient to improve analysis of 3D structures such as dendrites and spines, we analyzed 3D image stacks taken through fluorescent beads and spiny stretches of dendrite (Figure 5). Maximal intensity projections of 200 nm fluorescence beads again revealed improved resolution, reflected by decreased FWHM of the projected image from 420 nm to 240 nm (Figure 5A). Furthermore, surface rendering of the 3D image stack confirmed that the reduced fluorescence spread with STED 2PLSM was maintained in out-of-focus planes, allowing improved separation of objects throughout their 3D extent (Figure 5B). Similar surface rendering of deconvolved image stacks of spiny regions of dendrite (Figures 5C and 5D) indicated improved discrimination of morphological features including the ability to distinguish tightly packed structures and resolve spine necks. Furthermore, even within this highly complex 3D fluorescence distribution the increased resolving power of STED 2PLSM allows improved identification of morphological features within each plane of the undeconvolved images stack (Figures 5E and 5F).

To further quantify the ability of STED 2PLSM to resolve the fine features of dendrites of living neurons, we measured the dimensions of dendritic spines in 3D images stacks acquired by 2PLSM with and without STED (Figure 6). As expected, greater morphological detail of spines was clearly visible in maximal intensity projections of highly spiny dendritic regions (Figure 6A). For each spine, the spine length, spine head width, and spine head cross-sectional area were measured (Figures 6B and 6C). Dimensions that are accurately captured by 2PLSM are expected to be quantitatively unchanged under 2PLSM STED, whereas those that are significantly blurred by 2PLSM should appear smaller with 2PLSM STED. For each spine (n = 36), length was similar under 2PLSM and STED 2PLSM (STED 2PLSM length = 650 ± 35 nm; 2PLSM length = 649 ± 35 nm, $p > 0.05$; Wilcoxon signed-rank) whereas the spine head width (STED 2PLSM, width = 366 ± 15 nm; 2PLSM, width = 436 ± 17 nm, $p < 0.001$; Wilcoxon signed-rank) and area (STED 2PLSM, area = 0.22 ± 0.02 μm^2; 2PLSM, area = 0.30 ± 0.02 μm^2, $p < 0.0001$; Wilcoxon signed-rank) were significantly less with STED 2PLSM (Figure 6E). In addition, compared to conventional 2PLSM, under STED 2PLSM the fluorescence intensity of spine heads relative to that of the dendrite increased 23.2%, as expected for small structures imaged with improved resolution (STED 2PLSM, spine head/dendrite fluorescence ratio = 0.35 ± 0.17; 2PLSM,

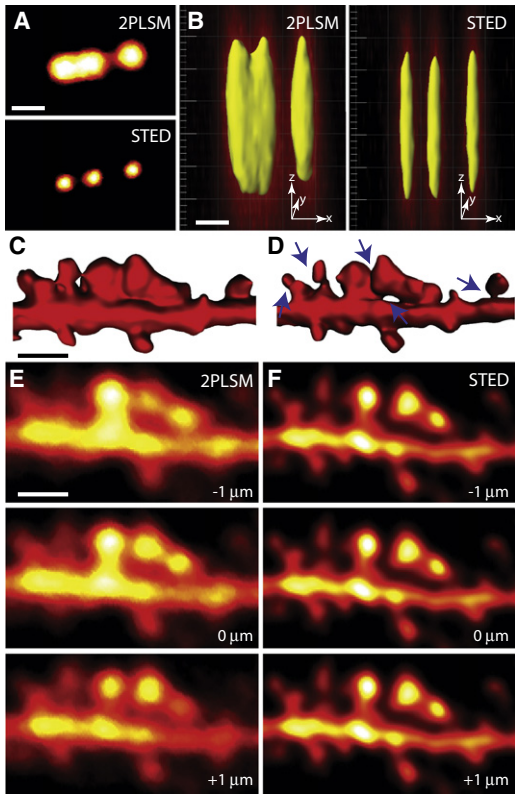

Figure 5. 3D Reconstruction of 2PLSM and STED 2PLSM Images

(A) Maximum intensity axial (z) projections of image stacks of fluorescent 200 nm crimson beads acquired with 2PLSM (top) and STED 2PLSM (bottom). Slice spacing = 200 nm.

(B) 3D reconstruction of the beads shown in (A). The 2PLSM images of the left-most beads are fused along the entire z extent of the image stack whereas they are clearly distinct throughout the stack in the STED 2PLSM images.

(C and D) 3D surface rendering of a segment of dendrite and spines collected as an image stack (500 nm spacing, 12 slices) acquired with 2PLSM (C) and STED 2PLSM (D). The arrows indicate details in the STED rendering that are not resolved in 2PLSM. These include features of the spine heads, separations between structures, and spine necks.

(E and F) Sample individual slices of the image stack rendered in (C and D) acquired at different focal planes with 2PLSM (E) and STED 2PLSM (F). Scale bars, 500 nm in (A) and (B), 2 µm in (C)–(F).

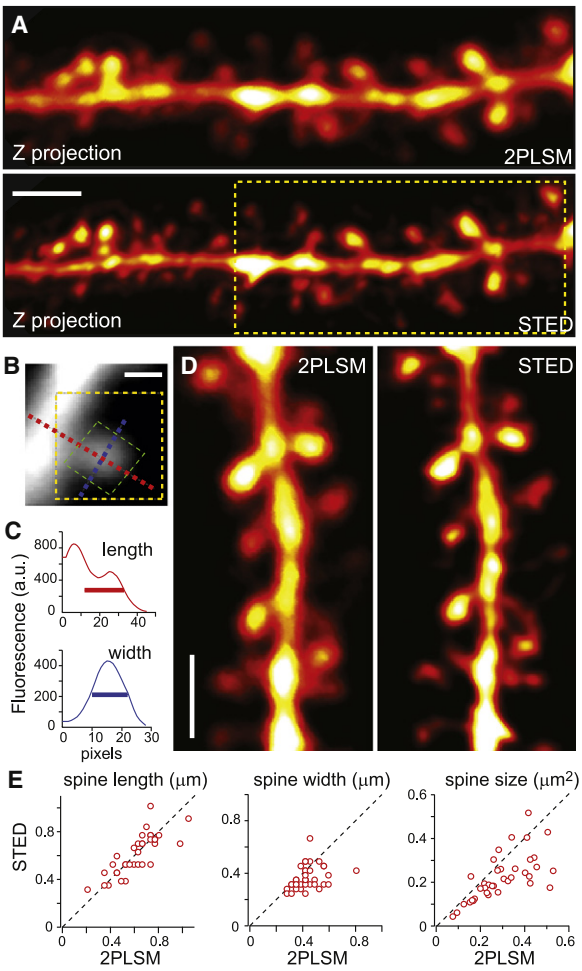

Figure 6. Quantitation of Dimensions of Dendritic Spines Imaged using STED 2PLSM

(A) Maximum intensity projection of image stacks of dendrite and spines acquired with 2PLSM (top) and STED 2PLSM (bottom). Scale bar, 2 µm.

(B) Image of an individual dendritic spine indicating the method of morphometric analysis. The major (red line) and intersecting minor (blue line) axes were marked along the length and the width of the spine. The green box indicates the area containing the spine head. The pixels within this box whose fluorescence intensities are at least 50% of the maximal value are used to define the area of the spine head. Scale bar, 500 nm.

(C) The distances to 50% of maximal fluorescence along the major and minor axis were used to define, respectively, the apparent spine length (thick red line) and head width (thick blue line).

(D) Enlarged single slice across the center of the image stacks shown in (A) acquired with 2PLSM (left) and STED 2PLSM (right). Scale bar, 2 µm.

(E) Comparison of spine length (left), head width (middle), and head area (right) measured from images shown in (A) collected with STED 2PLSM (y axis) and 2PLSM (x axis). The spine lengths are similar in both imaging modes whereas the head widths and areas are, as expected with improved imaging resolution, smaller with STED 2PLSM than 2PLSM.

0.30 ± 0.18, $p < 0.0001$; Wilcoxon signed-rank). Thus, the improved lateral resolution of STED 2PLSM significantly increases the ability to measure dimensions of dendritic spines in brain slices.

One of the avenues of research made possible by 2PLSM has been the analysis of developmental and activity-dependent plasticity of dendritic spines in living animals and in brain slices (Tanaka et al., 2008; Trachtenberg et al., 2002). Since STED 2PLSM was implemented using a high-power CW laser, we examined if potential phototoxicity would prevent repetitive time-lapse imaging of the same dendrite (Figure 7). The images show typical results of seven repeated images of the same dendritic region taken quickly over an 8 min time window with 2PLSM and STED 2PLSM. No evidence of photodamage was detectable and all STED 2PLSM images consistently exhibited separation of clustered spines that were not resolvable by 2PLSM. Furthermore, since the fluorophore in these experiments is a freely diffusing small molecule, photobleaching of the structure is not evident over time. Lastly, quantitative analysis of spine morphology during repetitive imaging at 1 min intervals revealed little change in spine length, head width, and head

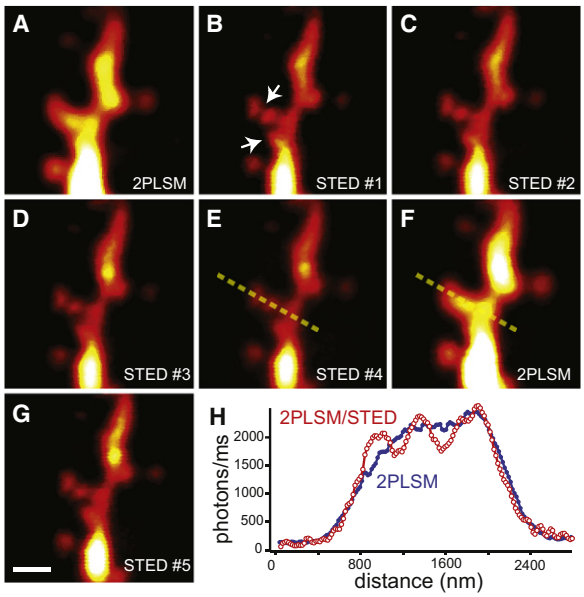

Figure 7. Repeated STED 2PLSM Imaging of Dendrites in Brain Slices

(A–G) Multiple images of an Alexa 594 loaded dendritic segment acquired with 2PLSM (A and F) and STED 2PLSM (B–E and G). The arrows indicate details in the STED 2PLSM image that are repeatedly resolved despite prolonged imaging. Scale bar, 1 μm. The dendrite was at an approximate depth of 80 μm in the slice.

(H) The profile of fluorescence intensity along the dashed lines in (E) and (F) exhibits separation of clustered spines in the STED 2PLSM mode (red) but not in the 2PLSM mode (blue).

cross-sectional area over time, consistent with a lack of significant photodamage (Figure S5).

DISCUSSION

The diffraction limit has been broken by several "super-resolution" microscopy techniques, including saturated structured illumination microscopy (SSIM) (Gustafsson, 2005), stochastic optical reconstruction microscopy (STORM) (Rust et al., 2006), photoactivated localization microscopy (PALM) (Betzig et al., 2006), and STED (Hell and Wichmann, 1994). Each of these approaches has its own limitations. SSIM, STORM, and PALM require mathematical postprocessing and image reconstruction as well as prolonged imaging of each specimen. Moreover, these three approaches are degraded by spherical aberrations and scattering of emitted photons, generally limiting their utility to thin specimens. STED microscopy uses a purely physical process and is a scanning imaging approach, allowing repeated examination of moving small objects within living cells (Westphal et al., 2008). However, STED has thus far only been implemented using one-photon excitation by visible light, preventing its use within scattering tissues such as the brain. Consequently there currently exists no supraresolution approach applicable to live-cell imaging below the surface of brain tissues.

We have demonstrated that STED 2PLSM is capable of imaging neuronal structures deep in brain tissues with resolution beyond the Abbe diffraction limit. In our experiments, ~3-fold improvement in radial resolution was achieved when imaging at depths of ~100 microns in brain slices. Further improvements in resolution will be achieved by more efficient delivery of the STED laser light, both by use of improved optics and by use of a pulsed depletion laser. The latter requires that the STED laser pulses arrive at the specimen precisely after the excitation pulse for optimal depletion of the excited state. Compared to continuous-wave STED described here, pulsed depletion should use STED laser power approximately 10-fold more efficiently. According to the theoretically predicted resolution of STED microscopy (Equation 1), this will allow ~10-fold improvements in resolution below the diffraction limit, reaching ~50 nm within brain tissue.

The utility of STED 2PLSM for deep tissue imaging arises from the use of multiphoton excitation and near infrared light. The use of near infrared light allows the formation of a focus deep within tissue that would degrade a visible light focus through scattering and absorption. Multiphoton excitation constrains fluorophore excitation to a small focal volume, eliminating out-of-focus fluorescence (Denk and Svoboda, 1997). This obviates the need for a descanned pinhole in the fluorescence detection path, thus permitting the use of scattered emission photons for image formation. For these reasons, STED 2PLSM using NIR excitation and depletion light is theoretically useful for deep tissue supraresolution imaging. We demonstrate that, in practice, spherical aberrations due to index of refraction mismatches, forward scatter of excitation photons, and phototoxicity are not significant obstacles to the implementation of STED 2PLSM.

In addition, we find that Alexa 594, a bright fluorophore used commonly in live cell and fixed tissue imaging, is suitable for STED 2PLSM. Alexa 594 has a low I_{sat} for CW STED such that, with our currently available laser power, $I_{max}/I_{sat} = 20$ and a 4- to 5-fold improvement in resolution should be possible. However, in our experimental measurements, we find an ~3-fold improvement in resolution (as judged from the FWHM of the thin structures). This apparent underperformance of STED 2PLSM compared to the theoretical limit may result from partial absorption of STED power by the tissue or from image degradation due to forward scatter of the excitation and STED beams. Conversely, it may be difficult to detect a 5-fold improvement in resolution in tissue due to the fact that our test imaging structures (dendritic spines and filopodia) were large (>100 nm; Bourne and Harris, 2008). We also find that STED 2PLSM with Alexa 594 is suitable for repeated time-lapse imaging because the small cytoplasmic fluorophore can readily diffuse and continuously replenish photobleached fluorophores. This is particularly important because, as the volume of excited fluorophores is reduced in STED imaging, the number of emitted photons is decreased and increased excitation laser power or averaging is required to maintain signal-to-noise ratios. Since Alexa 594 is an exceptionally bright and stable fluorophore, high-quality STED 2PLSM images can be achieved with low concentrations of fluorophore that are compatible with live cell imaging.

Several further improvements in STED 2PLSM are possible. First, as discussed above, more efficient use of STED power

will continue to improve the resolution to below 100 nm. Second, we have described improved resolution in the image plane but not in the axial plane. Improvements in axial resolution can be achieved through use of an annular, instead of helical, phase mask (Klar et al., 2000). Ideally both in plane and axial STED 2PLSM would be implemented simultaneously as has been demonstrated for conventional STED microscopy (Willig et al., 2007). Third, many genetically encoded red fluorophores, such as tdTomato and dsRed, have long fluorescent lifetimes (~3 ns) and long emission tails into the red spectrum (>700 nm), indicating that, if efficiently depleted, they may be suitable for STEP 2PLSM (Shaner et al., 2004). Lastly, identification of STED 2PLSM compatible synthetic and genetically encoded reporters of intracellular biochemical pathways, including calcium-sensitive fluorophores, may allow examination of intracellular signaling within functional microdomains.

With these advances, STED 2PLSM will be used for nanoscale imaging in relatively intact brain tissue to address fundamental questions in neuroscience. For example, indirect measurements suggest that the dimensions of each spine neck are rapidly regulated by activity of the associated synapse. However, it has been impossible thus far to accurately measure the spine neck in living neurons (Bloodgood and Sabatini, 2005; Grunditz et al., 2008; Tanaka et al., 2008). Second, activity-dependent regulation of ion channel trafficking and corralling (Choquet and Triller, 2003; Malinow and Malenka, 2002) is thought to be a principal mechanism of synaptic plasticity but direct measurements of protein movement at high resolution has not been possible in brain slices or in vivo. Third, spatially restricted biochemical signaling within subcellular microdomains is thought to confer specificity on calcium entry and kinase activation. However, direct measurement of the activity of biochemical pathways using fluorescence reporters has not been possible within microdomains. Lastly, STED 2PLSM will help resolve fine features of nonneuronal cells such as astrocytes, whose complex and intimate morphological relationship within neurons is only maintained in more intact preparations.

EXPERIMENTAL PROCEDURES

Two-Photon Laser Scanning STED Microscope

Imaging was accomplished using a custom made two photon laser scanning and STED microscope. The imaging laser is a mode-locked Ti:Sapphire laser (Chameleon, Coherent, Santa Clara, CA) tuned to 840 nm. The STED laser is a Ti:Sapphire laser (Mira/Verdi, Coherent, Santa Clara, CA) running in continuous wave mode at wavelengths of 736 nm and 760 nm for depletion of Alexa 594 and crimson fluospheres, respectively. The outputs of the lasers were independently modulated with Pockel's cells (350-80 and 350-50, Conoptics, Danbury, CT) and gated with mechanical shutters (VS25S2ZM1 and LS6Z2, Uniblitz, Vincent Associates, Rochester, NY). After expansion and collimation, the laser outputs were combined using a dichroic mirror (800SP, Chroma) and directed through a planoconvex lens (PCX150X25, Edmund Optics, Barrington, NJ) to a scanning galvanometer (6215H, Cambridge Technology, Cambridge, MA). Light reflected from the galvanometer was directed to a curved silver mirror (20DC100ER.2, Newport) that recollimated the beams and imaged the first galvanometer onto the second (6215H, Cambridge Technology, Cambridge, MA; Figure 2A). The scanning mirrors were imaged onto the back focal plane of the objective (63 X, 1.1 NA, Olympus, Melville, NY) with a scan lens (FV-PL-5I, Olympus) and tube lens (PLCX-50.8-91.2-UV-550/SLMF-0, CVI laser). This optical arrangement places both scan mirrors and the back-focal plane of the objective in conjugate optical planes and creates a stationary phase profile at the back-focal plane of the objective. In order to pattern the phase of the STED laser and create the doughnut-shaped intensity distribution in the specimen plane necessary for supraresolution imaging, a vortex phase plate (VPP-2, RPC Photonics) producing a helical phase retardation was introduced in the optical path after expansion of the STED laser.

Emitted fluorescence was collected by both epi and transfluorescence detectors. Short-pass dichroics (700DCXR) and interference filters (E700SP-2P) were used to eliminate excitation laser light. "Green" and "red" emitted photons were separated using a dichroic (565DCXR) and barrier filters (green, 525/50 Semrock; and red, 630/60, Chroma). Emitted photons were detected using photomultiplier tubes (H10770P-40MOD or R3896, Hamamatsu, Hamamatsu City, Japan). The current output of the trans- and epifluorescence detectors were combined at the input of trans-impedance preamplifiers (SR570, Stanford Research Systems) (one for each "color" channel). All filters and dichroics were from Chroma (Battleboro, VT) or Semrock (Rochester, NY).

Data Acquisition and Analysis

Imaging and physiology data were acquired using National Instruments boards and modified versions of ScanImage written in MATLAB (Mathworks) (Pologruto et al., 2003). The STED laser intensity was measured at the back aperture of the objective. Off-line analysis was performed using custom routines written in MATLAB and ImageJ (NIH). The pixel size of all images was 20 × 20 nm if not stated otherwise. Fluorescence intensities were analyzed using custom software written in Matlab (Mathworks) (Steiner et al., 2008). For each spine and time point, the user marked the major axis along the length of the spine and a minor axis intersecting the major axis at the point of maximal Alexa 594 fluorescence intensity in the spine head (Figure 6C). The distances to 50% of maximal fluorescence along the minor and major axis were used to define, respectively, the apparent head width and spine length. The area in which the fluorescence intensity of Alexa 594 remained above 50% of its maximal value was defined as the spine head mask, and the number of pixels within it defined the spine head area. The frame rate was 256 ms/frame (for 128 × 128 images) to 1024 ms/frame (for 512 × 512 images). Images and image stacks ($\Delta z = 0.2$ to 1 μm, typically 16 to 40 image sliced) were acquired repeatedly at variable time points (typically at maximal frame rate or at 1 min intervals). For 3D surface rendering, image stacks were first deconvolved using Huygens Professional (Scientific Volume Imaging) and plotted using Imaris (Bitplane).

The data are presented as mean ± SEM and $p < 0.05$ was considered as statistically significant.

Live Cell Labeling and Imaging

Horizontal slices (300 μm thick) were cut from the hippocampus of 15- to 19-day-old C57BL6 mice in ice-cold ACSF containing (in mM) 125 NaCl, 2.5 KCl, 2 $CaCl_2$, 1 $MgCl_2$, 25 $NaHCO_3$, 1.25 NaH_2PO_4, 25 glucose, bubbled with 95 % O_2 and 5 % CO_2. After a 30 min incubation at 34°C, slices were stored in ACSF at room temperature (22°C–23°C) until use. Individual slices were transferred to a submersion-style recording chamber and continuously superfused with ACSF at a rate of 2–3 ml/min at room temperature. Whole-cell voltage-clamp recordings were performed using standard techniques. Recordings were performed on hippocampal CA1 pyramidal neurons visually identified in the slice with the help of infrared-differential interference contrast (IR-DIC) video microscopy with a Hamamatsu camera/controller system (Hamamatsu, Japan). Recording pipettes (3–5 MΩ) were filled with Cs^+ internal solution containing the following (in mM): 120 $CsMeSO_3$, 15 CsCl, 8 NaCl, 10 TEA-Cl, 10 HEPES, 2–5 QX-314, 0.2 EGTA, 2 Mg-ATP, 0.3 Na-GTP (pH 7.3) adjusted with CsOH. One hundred micromolar Alexa Fluor 594 was added in the internal solution for imaging of neuronal morphology.

SUPPLEMENTAL DATA

Supplemental Data include five figures and can be found with this article online at http://www.cell.com/neuron/supplemental/S0896-6273(09)00518-2.

ACKNOWLEDGMENTS

The authors thank Andrew Giessel and Dr. Matthew Banghart for assistance in preparing samples and members of Sabatini laboratory for helpful discussions. The authors thank Sarah R. Jensen and Ian Oldenburg for assistance in producing the cover illustration.

Accepted: July 15, 2009
Published: August 26, 2009

REFERENCES

Abbe, E. (1873). Beitrage zur Theorie des Mikroskops und der mikroskopischen Wahrnehmung. Archiv fur Mikroskopische Anatomie *9*, 413–420.

Betzig, E., Patterson, G.H., Sougrat, R., Lindwasser, O.W., Olenych, S., Bonifacino, J.S., Davidson, M.W., Lippincott-Schwartz, J., and Hess, H.F. (2006). Imaging intracellular fluorescent proteins at nanometer resolution. Science *313*, 1642–1645.

Bloodgood, B.L., and Sabatini, B.L. (2005). Neuronal activity regulates diffusion across the neck of dendritic spines. Science *310*, 866–869.

Bourne, J.N., and Harris, K.M. (2008). Balancing structure and function at hippocampal dendritic spines. Annu. Rev. Neurosci. *31*, 47–67.

Choquet, D., and Triller, A. (2003). The role of receptor diffusion in the organization of the postsynaptic membrane. Nat. Rev. Neurosci. *4*, 251–265.

Denk, W., and Svoboda, K. (1997). Photon upmanship: why multiphoton imaging is more than a gimmick. Neuron *18*, 351–357.

Denk, W., Delaney, K.R., Gelperin, A., Kleinfeld, D., Strowbridge, B.W., Tank, D.W., and Yuste, R. (1994). Anatomical and functional imaging of neurons using two-photon laser scanning microscopy. J. Neurosci. Methods *54*, 151–162.

Eggeling, C., Ringemann, C., Medda, R., Schwarzmann, G., Sandhoff, K., Polyakova, S., Belov, V.N., Hein, B., von Middendorff, C., Schonle, A., and Hell, S.W. (2009). Direct observation of the nanoscale dynamics of membrane lipids in a living cell. Nature *457*, 1159–1162.

Grunditz, A., Holbro, N., Tian, L., Zuo, Y., and Oertner, T.G. (2008). Spine neck plasticity controls postsynaptic calcium signals through electrical compartmentalization. J. Neurosci. *28*, 13457–13466.

Gustafsson, M.G.L. (2005). Nonlinear structured-illumination microscopy: Wide-field fluorescence imaging with theoretically unlimited resolution. Proc. Natl. Acad. Sci. USA *102*, 13081–13086.

Hell, S.W., and Wichmann, J. (1994). Breaking the diffraction resolution limit by stimulated-emission - stimulated-emission-depletion fluorescence microscopy. Opt. Lett. *19*, 780–782.

Hell, S.W., Dyba, M., and Jakobs, S. (2004). Concepts for nanoscale resolution in fluorescence microscopy. Curr. Opin. Neurobiol. *14*, 599–609.

Kittel, R.J., Wichmann, C., Rasse, T.M., Fouquet, W., Schmidt, M., Schmid, A., Wagh, D.A., Pawlu, C., Kellner, R.R., Willig, K.I., et al. (2006). Bruchpilot promotes active zone assembly, Ca2+ channel clustering, and vesicle release. Science *312*, 1051–1054.

Klar, T.A., Jakobs, S., Dyba, M., Egner, A., and Hell, S.W. (2000). Fluorescence microscopy with diffraction resolution barrier broken by stimulated emission. Proc. Natl. Acad. Sci. USA *97*, 8206–8210.

Kner, P., Chhun, B.B., Griffis, E.R., Winoto, L., and Gustafsson, M.G. (2009). Super-resolution video microscopy of live cells by structured illumination. Nat. Methods *6*, 339–342.

Lee, S.J., Escobedo-Lozoya, Y., Szatmari, E.M., and Yasuda, R. (2009). Activation of CaMKII in single dendritic spines during long-term potentiation. Nature *458*, 299–304.

Lendvai, B., Stern, E.A., Chen, B., and Svoboda, K. (2000). Experience-dependent plasticity of dendritic spines in the developing rat barrel cortex in vivo. Nature *404*, 876–881.

Malinow, R., and Malenka, R.C. (2002). AMPA receptor trafficking and synaptic plasticity. Annu. Rev. Neurosci. *25*, 103–126.

Nagerl, U.V., Willig, K.I., Hein, B., Hell, S.W., and Bonhoeffer, T. (2008). Live-cell imaging of dendritic spines by STED microscopy. Proc. Natl. Acad. Sci. USA *105*, 18982–18987.

Pologruto, T.A., Sabatini, B.L., and Svoboda, K. (2003). ScanImage: flexible software for operating laser scanning microscopes. Biomed. Eng. Online *2*, 13.

Rust, M.J., Bates, M., and Zhuang, X. (2006). Sub-diffraction-limit imaging by stochastic optical reconstruction microscopy (STORM). Nat. Methods *3*, 793–795.

Sabatini, B.L., and Svoboda, K. (2000). Analysis of calcium channels in single spines using optical fluctuation analysis. Nature *408*, 589–593.

Shaner, N.C., Campbell, R.E., Steinbach, P.A., Giepmans, B.N., Palmer, A.E., and Tsien, R.Y. (2004). Improved monomeric red, orange and yellow fluorescent proteins derived from Discosoma sp. red fluorescent protein. Nat. Biotechnol. *22*, 1567–1572.

Shepherd, G.M., and Harris, K.M. (1998). Three-dimensional structure and composition of CA3→CA1 axons in rat hippocampal slices: implications for presynaptic connectivity and compartmentalization. J. Neurosci. *18*, 8300–8310.

Steiner, P., Higley, M.J., Xu, W., Czervionke, B.L., Malenka, R.C., and Sabatini, B.L. (2008). Destabilization of the postsynaptic density by PSD-95 serine 73 phosphorylation inhibits spine growth and synaptic plasticity. Neuron *60*, 788–802.

Svoboda, K., and Yasuda, R. (2006). Principles of two-photon excitation microscopy and its applications to neuroscience. Neuron *50*, 823–839.

Tanaka, J., Horiike, Y., Matsuzaki, M., Miyazaki, T., Ellis-Davies, G.C., and Kasai, H. (2008). Protein synthesis and neurotrophin-dependent structural plasticity of single dendritic spines. Science *319*, 1683–1687.

Trachtenberg, J.T., Chen, B.E., Knott, G.W., Feng, G., Sanes, J.R., Welker, E., and Svoboda, K. (2002). Long-term in vivo imaging of experience-dependent synaptic plasticity in adult cortex. Nature *420*, 788–794.

Tsai, S., Nishimura, N., Yoder, E.J., White, A., Dolnick, E., and Kleinfeld, D. (2002). Principles, Design and Construction of a Two Photon Scanning Microscope for In Vitro and In Vivo Studies (New York: CRC Press).

Westphal, V., Rizzoli, S.O., Lauterbach, M.A., Kamin, D., Jahn, R., and Hell, S.W. (2008). Video-rate far-field optical nanoscopy dissects synaptic vesicle movement. Science *320*, 246–249.

Willig, K.I., Rizzoli, S.O., Westphal, V., Jahn, R., and Hell, S.W. (2006). STED microscopy reveals that synaptotagmin remains clustered after synaptic vesicle exocytosis. Nature *440*, 935–939.

Willig, K.I., Harke, B., Medda, R., and Hell, S.W. (2007). STED microscopy with continuous wave beams. Nat. Methods *4*, 915–918.

Yan, Y., Hoffmann, H., Makarsky, A., Richter, W., and Talmon, Y. (2007). Swelling of Lalpha-phases by matching the refractive index of the water-glycerol mixed solvent and that of the bilayers in the block copolymer system of (EO)15-(PDMS)15-(EO)15. J. Phys. Chem. B *111*, 6374–6382.

Yuste, R., and Denk, W. (1995). Dendritic spines as basic functional units of neuronal integration. Nature *375*, 682–684.